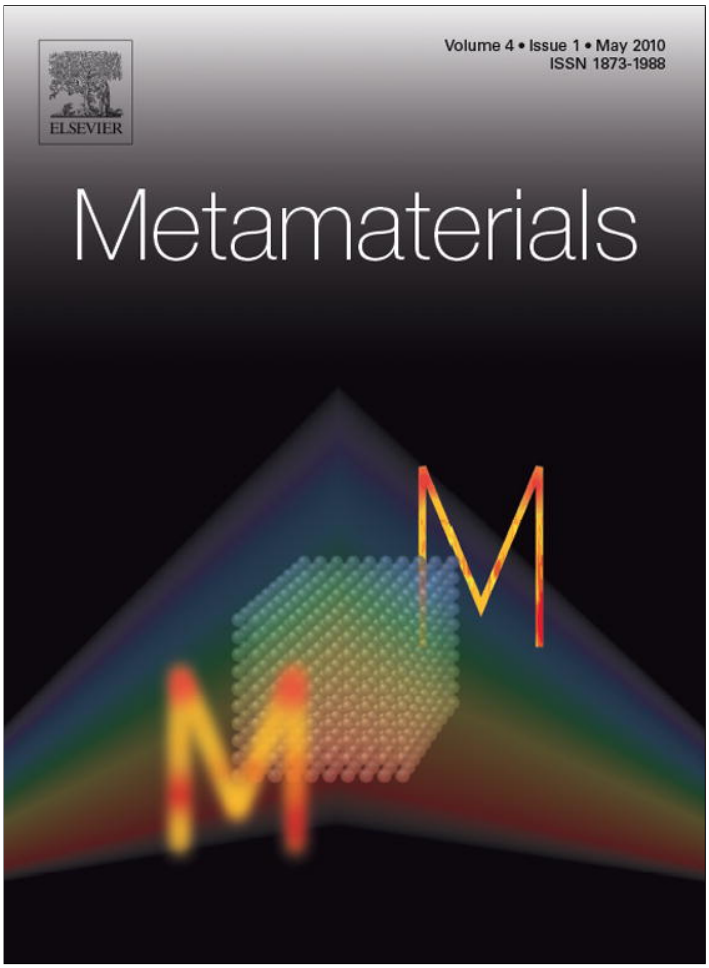

Available online at www.sciencedirect.com
ScienceDirect
Metamaterials 4 (2010) 1–14
Metamaterials
www.elsevier.com/locate/metmat

Flexible magnetoinductive ring MRI detector: Design for invariant nearest-neighbour coupling

R.R.A. Syms [a,*], T. Floume [a], I.R. Young [a], L. Solymar [a], M. Rea [b]

[a] *Optical and Semiconductor Devices Group, Electrical and Electronic Engineering Department, Imperial College London, Exhibition Road, London SW7 2AZ, UK*

[b] *Radiological Sciences Unit, Imperial College NHS Trust, MRI, St. Mary's Hospital, Praed St., Paddington, London W2 1NY, UK*

Received 24 September 2009; received in revised form 9 December 2009; accepted 9 December 2009
Available online 22 December 2009

Abstract

A flexible birdcage-type resonant RF detector for magnetic resonance imaging is described. The circuit consists of a polygonal ring of magnetically coupled *L–C* resonators, a periodic structure supporting backward magnetoinductive waves. The elements are mechanically linked to allow relative rotation, and the pivot point is optimised to hold the nearest-neighbour coupling coefficient invariant to small changes in the angle of an undistorted joint. Simple theory based on a parallel wire approximation to rectangular inductors is developed to allow the variation of the coupling coefficient with angle and radius to be estimated, and hence determine the location of the pivot. The optimised pivot is shown to reduce resonance splitting in octagonal rings. However, second-neighbour interactions degrade performance. The theory is verified experimentally using printed circuit board elements coupled by flexible hinges, and the invariance of the nearest-neighbour coupling coefficient is confirmed. Octagonal ring resonators are constructed for operation at 63.8 MHz frequency and the mode spectra of regular and distorted rings are measured. Magnetic resonance imaging properties are investigated using ^{1}H MRI of simple objects in a 1.5 T field. Images are obtained from undistorted and distorted resonators and the effect of distortion on SNR is quantified.

Keywords: Magnetoinductive wave; Metamaterial; Ring resonator; Magnetic resonance imaging; Birdcage coil

1. Introduction

The 'birdcage' RF detector, a circular resonant ladder network, is a workhorse of magnetic resonance imaging (MRI), providing an extended volume with uniform performance in transmission and reception [1,2]. Developments include high-frequency coils for high-field work [3], dual tuned coils for multi-nuclear detection [4,5] and elliptic coils for improved filling factor in head imaging [6,7]. Birdcage coils may be high-, low- or band-pass, depending on their equivalent circuit [8–10]. Alternative distinctions may be made in terms of the wave (forward or backward) supported by the ladder. Most birdcages employ both electrical and magnetic coupling between elements, the exception being the 'TEM' coil [11,12] which uses purely magnetic coupling and has the equivalent circuit of Fig. 1a.

Periodic electromagnetic structures are of considerable interest in the field of metamaterials, which aims to exploit the unusual properties (particularly, negative permittivity and/or permeability) of arrays of resonant elements (often, split-ring resonators) [13–17]. In this domain, waves propagating in arrays of magnetically

* Corresponding author. Tel.: +44 207 594 6203; fax: +44 207 594 6308.
E-mail address: r.syms@imperial.ac.uk (R.R.A. Syms).

1873-1988/$ – see front matter © 2010 Elsevier B.V. All rights reserved.
doi:10.1016/j.metmat.2009.12.001

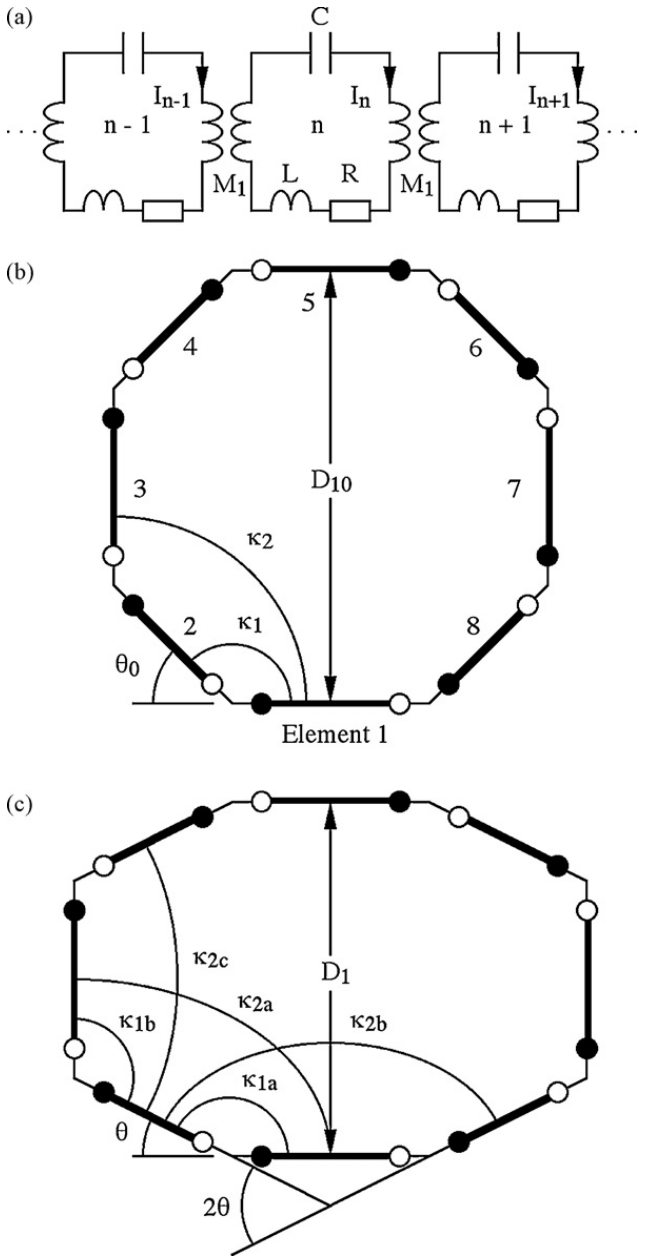

Fig. 1. Equivalent circuit of (a) a TEM coil or a magnetoinductive waveguide, (b) top view of an octagonal MI ring with rectangular elements and (c) symmetrically distorted ring.

coupled low-frequency resonators are termed "magnetoinductive" or MI waves [18–21]. Applications range from waveguides to filters and lenses [22–28]. Fig. 1a is also the equivalent circuit of a MI waveguide consisting of a regular arrangement of *L*–*C* resonators, each containing a capacitance *C* and an inductance *L* (with a series resistance *R*) and coupled to its nearest neighbour by a mutual inductance M_1. The properties of the wave are mainly determined by nearest-neighbour interactions, although non-nearest-neighbour coupling is unavoidable [23]. Forward and backward waves are obtained when M_1 is positive and negative, respectively.

When the loops are arranged in a polygonal ring, as shown in Fig. 1b, the MI wave will satisfy standard resonance conditions, namely that the phase shift round the ring must be a whole number of multiples of 2π. The primary mode can be coupled to the field of a rotating magnetic dipole in MRI, provided it is resonant at the correct frequency [29]. In this respect a MI ring is analogous to a birdcage coil, and parametrically amplified MI rings are now being developed [30–32]. However, because there is no rigid mechanical connection between adjacent elements, the MI approach should allow construction of a flexible ring, whose shape could be adjusted as in Fig. 1c.

Distortion of a magnetoinductive ring is likely to alter resonant frequencies. Furthermore, it may well degrade uniformity of signal reception because of the alteration in position and orientation of individual resonant elements. However, these disadvantages may be outweighed by increased sensitivity following from an improved filling factor in (for example) imaging of the human head.

Flexible transmission line array detectors have previously been developed for MRI using adjustable capacitances that automatically maintain de-coupling as the geometry alters [33]. Here we consider the alternative of a flexible MI ring containing a mechanism to stabilise mutual inductances so that the splitting of otherwise degenerate resonances caused by asymmetry is reduced. Clearly, it will be difficult to ensure that higher-order couplings are unaltered; however, rearrangement should hold at least the nearest-neighbour coupling fixed. Here we develop a mechanical link that allows changes in separation between elements to compensate for changes in angle [34,35]. Other applications lie in reducing discontinuities in curved metamaterial waveguides, which generate reflections.

This work should be seen in context with other important potential applications for metamaterials in MRI. These include flux-guides for transfer of images [36,37], yokes for concentration of flux [38,39], near-field lenses based on 'Swiss rolls' [40], split-ring resonators [41,42] and wires [43,44], and patient-safe cable for internal imaging [45,46].

In Section 2, we briefly review the properties of MI waves and ring resonators. In Section 3, we introduce a 2D model for the magnetic coupling between neighbouring elements. We develop approximations for its geometric dependence, and show that a displaced pivot can achieve stationary behaviour near a given design angle, the apex angle of an undistorted polygonal ring. In Section 4, we consider the theoretical performance of an octagonal ring, including the effect of higher-order coupling, and show that the compensating pivot outperforms a simple apex pivot. However, second-neighbour

interactions are shown to degrade performance. In Section 5, we verify the theory using printed circuit board (PCB) resonant elements and rings. In Section 6 we present the results of preliminary ^{1}H magnetic resonance imaging experiments and show that MR images may be obtained even from distorted resonators. Conclusions are presented in Section 7.

2. Magnetoinductive ring resonators

In this section, we briefly review the properties of magnetoinductive waves and MI ring resonators, previously described in [18,19,29], respectively.

2.1. Dispersion characteristics of magnetoinductive waves

For Fig. 1a, Kirchhoff's voltage law can be used to relate the current I_n in the nth element to those in its neighbours. At an angular frequency ω, and assuming travelling wave solutions $I_n = I_0 \exp\{j(\omega t - nka)\}$, where "$k$" is the propagation constant and "a" is the element separation, the dispersion equation for nearest-neighbour coupling may be obtained as:

$$\left\{1 - \frac{\omega_0^2}{\omega^2} - \frac{j}{Q}\right\} + \kappa_1 \cos(ka) = 0 \tag{1}$$

Here $\omega_0 = (LC)^{-1/2}$ is the angular resonant frequency, $Q = \omega_0 L/R$ is the quality factor and $\kappa_1 = 2M_1/L$ is the nearest-neighbour coupling coefficient. The complex propagation constant is $k = k' - jk''$, where $k'a$ and $k''a$ are the phase shift and attenuation per element, respectively. Eq. (1) may of course be solved exactly. However, for low losses, we may write:

$$\left(1 - \frac{\omega_0^2}{\omega^2}\right) + \kappa_1 \cos(k'a) \approx 0$$
$$k''a \approx \frac{1}{\kappa_1 Q \sin(k'a)} \tag{2}$$

The solution exists over the frequency band $1/(1+|\kappa_1|) \le (\omega/\omega_0)^2 \le 1/(1-|\kappa_1|)$ whose extent depends on the value of κ_1, and hence on M_1. Low losses require a high Q-factor and a high coupling coefficient, and losses are minimised at the band centre. High losses, which require a full solution, result in lossy propagation outside the band. For backward waves, $k''a$ is negative, and hence $|k''a|$ is the indicator of loss. Interactions between mth nearest neighbours may be modelled by introducing additional mutual inductances M_m and coupling terms κ_m into Eq. (1) to obtain [23]:

$$\left(1 - \frac{\omega_0^2}{\omega^2} - \frac{j}{Q}\right) + \sum_m \kappa_m \cos(mka) = 0 \tag{3}$$

2.2. Magnetoinductive ring resonators

A magnetoinductive ring resonator may be constructed from a polygonal arrangement of N coupled elements. Strong coupling may be achieved using closely spaced rectangular inductors. Fig. 1b shows a top view of such a ring (here, an octagon) which has each coil rotated by an angle $\theta_0 = 2\pi/N$ from its neighbours.

At the vertex joining the nth and $n+1$th element, the two parallel conductors perpendicular to the figure carry currents I_n and $-I_{n+1}$. At sufficient distance, the magnetic field created in a low-loss system is equivalent to a single conductor carrying a current:

$$I_{\text{eff}} = I_0\{\exp(-jnka) - \exp(-j[n+1]ka)\}$$
$$= I'_0 \exp\{-j(n+\tfrac{1}{2})ka\} \tag{4}$$

Here $I'_0 = 2jI_0 \sin(ka/2)$. The periodic arrangement of currents implies that the spatial distribution of magnetic field created by an energised ring will be similar to that of the corresponding conventional birdcage coil, but rotated in angle.

The ring will resonate when the phase shift round the ring is a whole number of multiples of 2π, so that $k'Na = 2\,\mu\pi$ where μ is the mode number. In a regular N-sided polygon, modal degeneracy implies that there will be fewer than N distinct resonant frequencies. For even N, there will be $N/2+1$ resonances, with propagation constants:

$$k'_\mu a = \frac{2\mu\pi}{N} \quad (\mu = 0, 1 \ldots, N/2) \tag{5}$$

Once the values of $k'_\mu a$ are known, the corresponding angular frequencies ω_μ may be obtained from the dispersion equation. In the low-loss case, Eqs. (3) and (5) give:

$$\frac{\omega_\mu}{\omega_0} = \left(1 + \sum_m \kappa_m \cos\frac{2\pi\mu m}{N}\right)^{-1/2} \tag{6}$$

The mode with $\mu = 1$ is the most significant for MRI applications, since it may couple to the field of a rotating magnetic dipole.

2.3. Distorted MI ring resonators

When the ring is distorted, the coupling coefficients will alter. Fig. 1c shows the most important terms for

the octagonal ring in Fig. 1b. There are now two possible nearest-neighbour coupling coefficients, κ_{1a} and κ_{1b}, and three second-nearest-neighbour terms, k_{2a}, k_{2b} and k_{2c}, whose differences will alter the resonant frequencies and mode patterns of the ring. One predictable consequence is a breaking of modal degeneracy. Since the largest coefficients are nearest-neighbour terms, the primary problem is to equalise κ_{1a} and κ_{1b}, by making κ_1 invariant to changes in apex angle. Symmetry implies that κ_{2a} must be inherently stationary for distortions of the type shown. Unfortunately, there is little that can be done to eliminate differences between κ_{2b} and κ_{2c}, or between higher-order coefficients. The best solution is therefore to maximise the relative size of the nearest-neighbour coefficient.

3. Flexible element link mechanism

The geometry of Fig. 1b really requires three-dimensional analysis to account for end effects. In this section, we develop a simpler two-dimensional theory that allows M_1, L and κ_1 to be estimated, and hence enables the design of a mechanism to hold κ_1 stationary to first order. Here we base the analysis on the approximate vertex geometry of Fig. 2a, in which each inductor is modelled by two infinite parallel wires of radius A and separation S and two adjacent inductors subtend a general angle θ at a centre a distance R away. This geometry is a realistic approximation to practical elements.

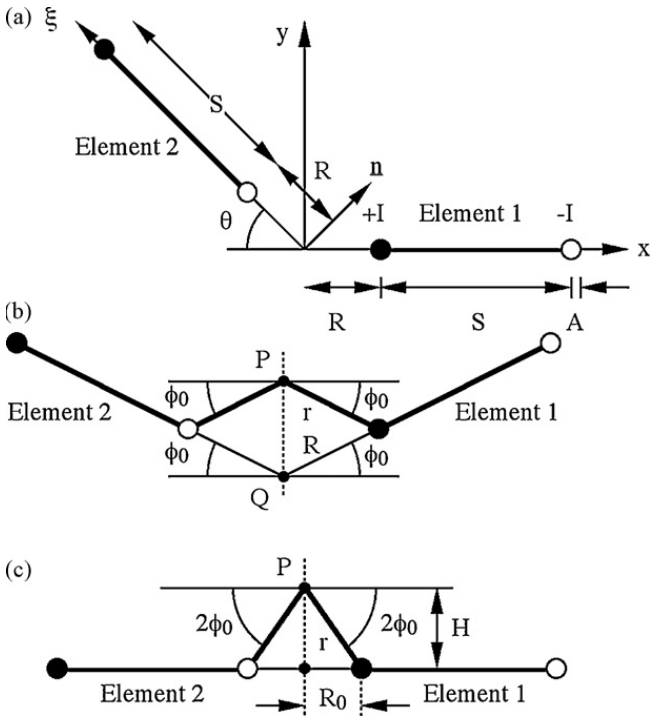

Fig. 2. Top view of (a) a single joint in a MI ring resonator, (b) a compensating joint at the design angle and (c) an unfolded compensating joint.

3.1. Nearest-neighbour coupling coefficient

The nearest-neighbour coupling coefficient can be found as follows. The flux density $\boldsymbol{B}$ at a point (x, y) created by a current I in inductor 1 is:

$$B_x = -\left(\frac{\mu_0 I}{2\pi}\right)\left\{\frac{y}{(x-R)^2+y^2} - \frac{y}{(x-R-S)^2+y^2}\right\}$$
$$B_y = +\left(\frac{\mu_0 I}{2\pi}\right)\left\{\frac{x-R}{(x-R)^2+y^2} - \frac{x-R-S}{(x-R-S)^2+y^2}\right\} \quad (7)$$

The component of $\boldsymbol{B}$ parallel to the normal vector $\boldsymbol{n}$ of inductor 2 is $B_n = \boldsymbol{B}\cdot\boldsymbol{n} = B_x\sin(\theta) + B_y\cos(\theta)$. Along the ξ-axis through element 2, $x = -\xi\cos(\theta)$ and $y = \xi\sin(\theta)$. Substituting, and rearranging we obtain:

$$B_n = -\left(\frac{\mu_0 I}{2\pi}\right)\left\{\frac{\xi + R\cos(\theta)}{[\xi + R\cos(\theta)]^2 + R^2\sin^2(\theta)}\right\}$$
$$+\left(\frac{\mu_0 I}{2\pi}\right)\left\{\frac{\xi + (R+S)\cos(\theta)}{[\xi + (R+S)\cos(\theta)]^2 + (R+S)^2\sin^2(\theta)}\right\} \quad (8)$$

The total flux passing through inductor 2 per unit length (p.u.l.) is $\Phi_{12} = {}_{R+A}\int^{R+S-A} B_n\,\mathrm{d}\xi$. Integrating, we can obtain the mutual inductance per unit length $M_1 = \Phi_{12}/I$ as:

$$M_1 = -\frac{\mu_0}{4\pi}\ln\left\{(\xi + R\cos\theta)^2 + R^2\sin^2\theta\right\}\Big|_{R+A}^{R+S-A}$$
$$+\frac{\mu_0}{4\pi}\ln\left\{(\xi+(R+S)\cos\theta)^2 + (R+S)^2\sin^2\theta\right\}\Big|_{R+A}^{R+S-A} \quad (9)$$

The self-inductance per unit length L may be found by similar methods, as:

$$L = \left(\frac{\mu_0}{\pi}\right)\ln\left\{\frac{S-A}{A}\right\} \quad (10)$$

The nearest-neighbour coupling coefficient κ_1 may then be estimated using Eqs. (9) and (10). Its value is negative, and its modulus increases slowly with θ from a stationary point at $\theta = 0$. This variation implies that a pivot located exactly at each vertex will not provide the required behaviour in a flexible polygonal ring. We now develop a more appropriate design.

3.2. Mechanism design

If $S \gg R$ and $R > A$ (as is generally the case) the mutual inductance per unit length is approximately:

$$M_1 \approx -\left(\frac{\mu_0}{2\pi}\right)\ln\left\{\frac{S}{2R\{1+\cos(\theta)\}}\right\}$$
$$= -\left(\frac{\mu_0}{2\pi}\right)\ln\left\{\frac{S}{4R\cos^2(\phi)}\right\} \quad (11)$$

Here, $\phi = \theta/2$. Under similar conditions, $L \approx (\mu_0/\pi)\ln(S/A)$, allowing the nearest-neighbour coupling coefficient to be estimated as:

$$\kappa_1 \approx -\frac{\ln\{S/[4R\cos^2(\phi)]\}}{\ln(S/A)} \quad (12)$$

Eq. (12) implies that the coupling coefficient is a function of R and ϕ. However, if R is altered to compensate for changes in ϕ, κ_1 may be held constant. Clearly, the required variation is $R(\phi) = R_0/\cos^2(\phi)$, where R_0 is the value of R at $\theta = 0$. This variation must be obtained using a mechanical arrangement linking the two inductors. To avoid interference with the subject in an imaging application, the mechanism must be compact. It must also be low cost, since an identical mechanism must be provided at each vertex. We have therefore concentrated on a simple pivot that holds κ_1 approximately constant over a limited range.

Fig. 2b shows an alternative view of the vertex, in which the inductors are arranged on either side of a dashed line of symmetry, on which any such pivot must lie. Here the pivot point P is arranged so that the radius arm (of length r) makes an angle ϕ_0 to the inner conductor of each coil, when the half-angle at the apex at Q is also ϕ_0. If inductor 1 (say) is rotated counter-clockwise to a new angle ϕ such that $\phi = \phi_0 + \Delta\phi$, the angle of the radius arm must alter to $\phi_0 - \Delta\phi$. Simple geometry then implies that

$$R = \frac{r\cos(\phi_0 - \Delta\phi)}{\cos(\phi_0 + \Delta\phi)} \quad (13)$$

Assuming that $\Delta\phi$ is a small angle, we obtain after some manipulation:

$$R \approx \frac{r}{1 - 2\Delta\phi\tan(\phi_0)} \approx \frac{r\cos^2(\phi_0)}{\cos^2(\phi)} \quad (14)$$

Eq. (14) implies that an approximation to the desired variation is indeed obtained for small changes in angle. Fig. 2c shows the joint rotated so that the inductors are now coplanar. The length of radius arm is $r = R_0/\cos(2\phi_0)$, and the joint may be constructed by placing a hinge at a height $H = R_0\tan(2\phi_0)$ above the plane of the inductors.

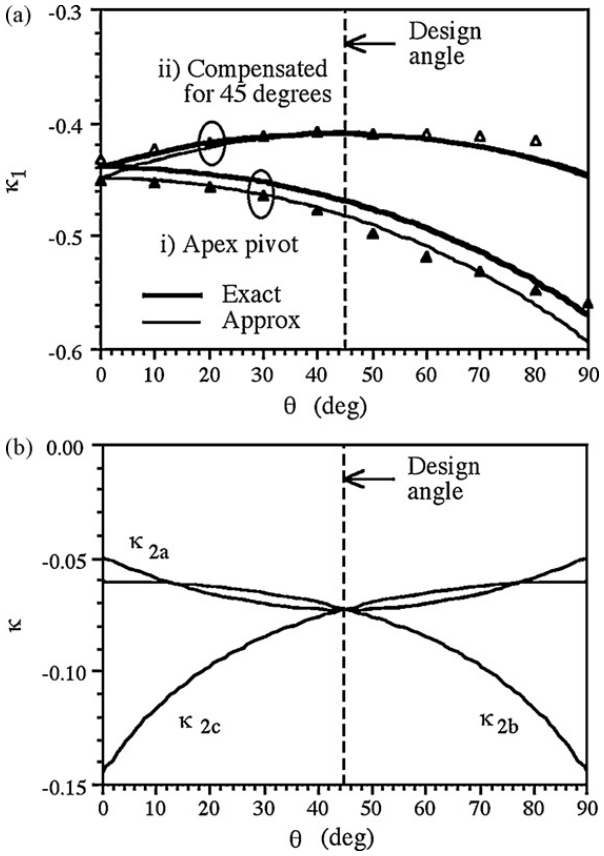

Fig. 3. (a) Variation of the nearest-neighbour coupling coefficient with angle θ, for pivots at (i) Q and (ii) P, assuming $N = 8$. Thick lines show the result of exact theoretical expressions for M_1, thin lines show approximate results and points show experimental data. (b) Theoretical variation of the second nearest-neighbour coupling coefficients with θ for a distorted octagonal ring. In each case, $A = 0.5$ mm, $R_0 = 1.75$ mm, and $S = 60$ mm.

3.3. Numerical verification

We now verify the analysis above with a simple example. Fig. 3a shows predictions for the angular variation in coupling coefficient for pivots at (i) the apex Q and (ii) the optimum location P, assuming the design angle $\theta_0 = \pi/4$ of an 8-element ring. In each case, the typical parameters $A = 0.5$ mm, $R_0 = 1.75$ mm and $S = 60$ mm are assumed, for later comparison with the experimental data points shown, and two curves are presented. Thick lines show predictions of the exact expression for M_1, while thin lines show values from the approximation used to locate the pivot. Since there is good agreement between the two, the latter is used from now on.

With the pivot at Q, $|\kappa_1|$ increases monotonically with θ, and this variation would clearly alter the resonant behaviour of the ring as it flexed. However, when the pivot is moved to the compensating position P, the coupling coefficient shows stationary behaviour near the design angle as required. The working range appears to

be at least ±10°, which should allow considerable distortion. This result has been achieved at a price; the value of $|\kappa_1|$ is lower for the compensating pivot, because a larger initial separation is required between the elements to allow the gap between them to close as θ is reduced.

The analysis above has made numerous approximations. However, the main conclusion is likely to be true even in a more realistic inductor geometry, namely that first-order compensation for changes in angle may be obtained by appropriate changes in separation.

4. Flexible polygonal magnetoinductive ring

In this section, we consider the theoretical performance of a flexible polygonal MI ring. The new aspects to consider are the allowed geometric distortions and the detailed variation of nearest- and additional non-nearest-neighbour coupling coefficients. All have a cumulative effect on the resonant modes. To simplify the analysis, we restrict changes in geometry to symmetric distortion of an octagonal ring as shown in Fig. 1c. In this case, the shape of the ring is defined by the single variable θ, and changes in element orientation and position are predictable; alternate elements either translate or rotate, but not both. There are two axes of symmetry, and symmetrically located elements displace in opposite senses.

4.1. Coupling coefficients

With these geometric assumptions, the angle at each vertex must either be θ or $\pi/2-\theta$, so that only two different nearest-neighbour coefficients κ_{1a} and κ_{1b} need be considered. For apex pivots, κ_{1a} varies as curve (i) in Fig. 3a, while the variation of κ_{1b} is simply a mirror image of this curve about $\theta_0=\pi/4$. For compensating pivots, with the assumption of Eq. (11), it is simple to show that $\kappa_{1a}=\kappa_{1b}$ for all angles, and that both coefficients vary as curve (ii) in Fig. 3a. This variation is symmetric about $\theta_0=\pi/4$.

Again, for simplicity, we restrict the discussion of non-nearest effects to second neighbours. If the distance R and its variation with angle are both neglected (since R is small compared with the separation of second neighbours), the three different second-neighbour coefficients κ_{2a}, κ_{2b} and κ_{2c} may easily be calculated using the methods of the previous section. All that is required is to define the relative angles of the elements appropriately using Fig. 1c (in the calculation for κ_{2b} and κ_{2c}) and to shift the relative positions of the elements (for κ_{2a}). The algebra is simple but lengthy, so we present the results numerically.

Fig. 3b shows the angular variations of κ_{2a}, κ_{2b} and κ_{2c}, calculated assuming the same parameters as before. When $\theta=\pi/4$, all three coefficients are equal, as expected from symmetry. As θ changes, the coefficient values alter. The variation of κ_{2a} is symmetric about $\theta=\pi/4$, while the variations of κ_{2b} and κ_{2c} are mirror images about this point. The secondary coefficients are surprisingly large, between 1/5 and 1/6 of the primary coefficients when $\theta=\pi/4$ and increasing significantly as θ alters from this value. We have verified numerically that the second-neighbour coefficients are insensitive to small changes in the first-neighbour pivot design, validating the geometric approximations used.

4.2. Resonant frequencies

Given numerical values of the coupling coefficients, the resonant frequencies of the ring may be estimated. There are two approaches. For an undistorted ring, the coefficients are constant and Eq. (6) may be used. For

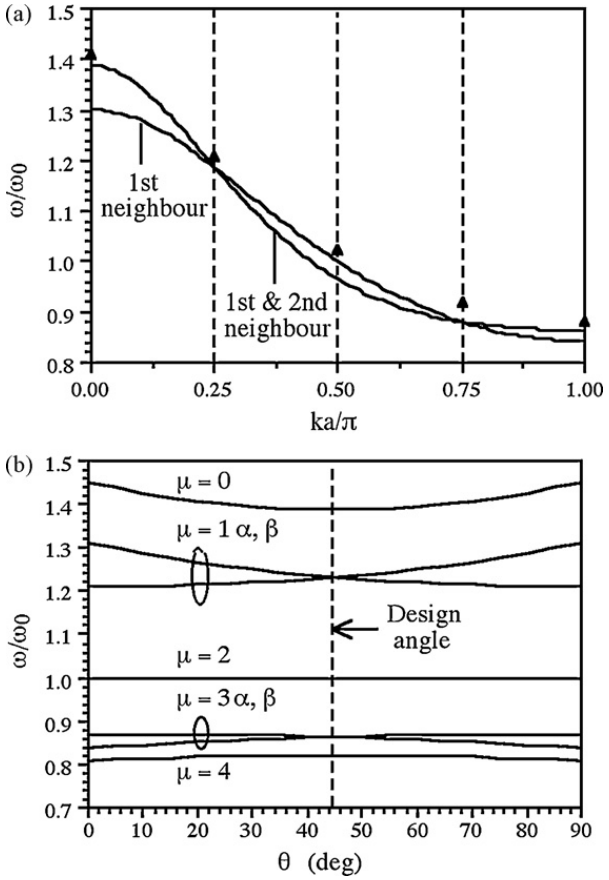

Fig. 4. (a) ω–k diagram of undistorted octagonal ring resonator. Lines show theoretical results assuming two different models for the dispersion characteristic; points show experimental data. (b) Theoretical variation of the entire set of mode frequencies with θ for a distorted octagonal ring with apex pivots, assuming nearest-neighbour coupling only. In each case, parameters are as Fig. 3.

the distorted ring, the coefficients vary with the element number. Kirchhoff's law must therefore be used for each element, and the resulting set of coupled equations solved to find the resonant frequencies.

Fig. 4a shows the normalised resonant frequencies of an undistorted octagonal ring, plotted on a ω–k diagram. The allowed resonances are the five intersections of the dispersion curve with dashed lines through $ka = \mu\pi/4$, with $\mu = 0, 1, \ldots, 4$. Two alternative variations are shown, the first assuming nearest-neighbour coupling only and the second including both first- and second-neighbour terms. In each case, the parameters used are the same as before. Inclusion of second-neighbour terms alters the dispersion characteristic significantly, especially for low values of ka.

Fig. 4b shows the variation with θ of the resonant frequencies of an octagonal ring with apex pivots, found by numerical solution of the eigenvalue problem for nearest-neighbour coupling only. When $\theta = \pi/4$, there are five resonances. However, as the value of θ alters, the resonances $\mu = 1$ and $\mu = 3$ each split into two modes (labelled 'α' and 'β'), destroying modal degeneracy. The effect is most significant for the primary mode, which we now focus on. Note that when $\theta = 0°$ or $\theta = 90°$, the ring is actually rectangular rather than octagonal. The effect of interactions of higher order than those considered here (particularly, 4th order) may then be entirely non-negligible. Consequently only the central region of the plot near $\theta = 45°$ is likely to provide a truly accurate prediction of mode splitting.

Fig. 5a compares the angular variation of the two primary mode frequencies obtained with apex and compensating pivots, again assuming nearest-neighbour coupling only. At $\theta = \pi/4$, the resonant frequencies differ slightly, due to differences in the coupling coefficient obtained with the two pivot designs. More importantly, the splitting of the primary mode is entirely prevented by the compensating pivot. Instead, the resonant frequency rises slowly away from $\theta = \pi/4$, due to the gradual change in coupling coefficient in curve (ii) of Fig. 3a. At this level of approximation, the compensating pivot therefore operates well.

Fig. 5b shows similar results, now calculated assuming both first- and second-neighbour interactions. The additional coupling terms increase the mode splitting seen with the apex pivot, and introduce a smaller amount of splitting despite the use of a compensating pivot. When higher-order effects are included, the compensating pivot therefore works less well. However, improved performance would be expected if the elements can be placed closer together so that the nearest-neighbour coupling is increased, and if the number of elements N can be increased so that second-neighbour interactions reduce.

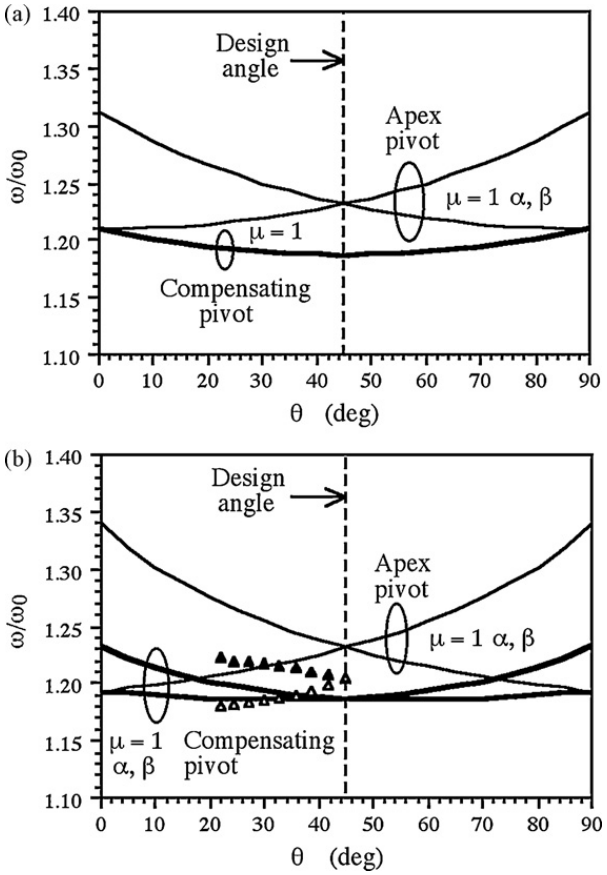

Fig. 5. Theoretical variation of the two primary mode frequencies with θ for distorted octagonal rings with apex and compensating pivots, assuming (a) nearest-neighbour coupling only, and (b) both nearest and second nearest-neighbour coupling. In each case, parameters are as Fig. 3. Black and white triangles show experimental data for apex and compensating pivots, respectively.

5. Experimental verification

In this section, we investigate the validity of the previous theory experimentally, using resonant elements and MI ring resonators constructed from PCBs.

5.1. Resonant elements

Experiments were carried out with elements based on non-magnetic FR-4 PCBs, using an Agilent E5061A network analyser for characterisation. Single-turn rectangular inductors with long conductors close to the PCB edge were used to achieve high Q-factor and high nearest-neighbour coupling, and element sizes were chosen to yield rings approximately 2/3 the size of a conventional head coil. With a span $S = 60$ mm, a track length of 180 mm, and a track width and thickness of

$2A = 1$ mm and 85 μm, respectively, a self-inductance of ≈0.5 μH was obtained. The resonant frequency of isolated elements was chosen to locate the primary resonance of an octagonal ring at 63.8 MHz, the operating frequency of ^{1}H MRI in a 1.5 T magnetic field. With the addition of 16.5 pF capacitors, a resonant frequency of $f_0 = \omega_0/2\pi \approx 53$ MHz and a Q-factor of 130 were obtained.

5.2. Coupling coefficients

Coupling coefficients were determined by the split resonance method, in which the resonant frequencies of a symmetric coupled LC resonator system are used to derive the ratio between the self and mutual inductances [29,30]. Two identical resonators are mounted at appropriate spacing and orientation, and the eigenfrequencies f_s and f_a of the symmetric and antisymmetric modes of the coupled system were measured using a weak inductive probe. The modes themselves were identified from the relative signal phase in the two oscillators, and the coupling coefficient was estimated as $\kappa = -2\{1 - f_0^2/f_s^2\} = +2\{1 - f_0^2/f_a^2\}$.

The variation of the coupling coefficient was first found for an apex pivot. To do so, two elements were mounted in a Perspex stage that allowed one to be fixed and the other rotated through a known angle, as shown in Fig. 6a. The earlier Fig. 3a shows the measured variation of κ_1 with θ for a pair of elements with $R_0 \approx 1.75$ mm. The qualitative agreement with the model is excellent, but there are discrepancies for larger values of θ. These differences are ascribed to a slight 'bow' in the PCBs, which caused their separation to increase at larger angles. The second-neighbour coupling coefficient was also measured. For a fixed angle of $\theta_0 = 45°$, the value of κ_2 was around 1/7 of the value of κ_1.

5.3. Link mechanism

The variation of the nearest-neighbour coupling coefficient was then found for an optimised pivot. Hinges were constructed as flexure elements by milling V-shaped grooves into short sections of Delrin (polyoxymethylene, an engineering thermoplastic from Dupont that can easily be machined to form precision parts but that has sufficient flexibility for this application). The hinges were attached to the PCBs with nylon bolts as shown in Fig. 6b, using thin spacers to set the height H. Five flexures were used per element as shown in Fig. 6c, eliminating most of the 'bow' described above. The earlier Fig. 3a also shows the angular variation of κ_1 obtained with the spacer optimised for a design angle of

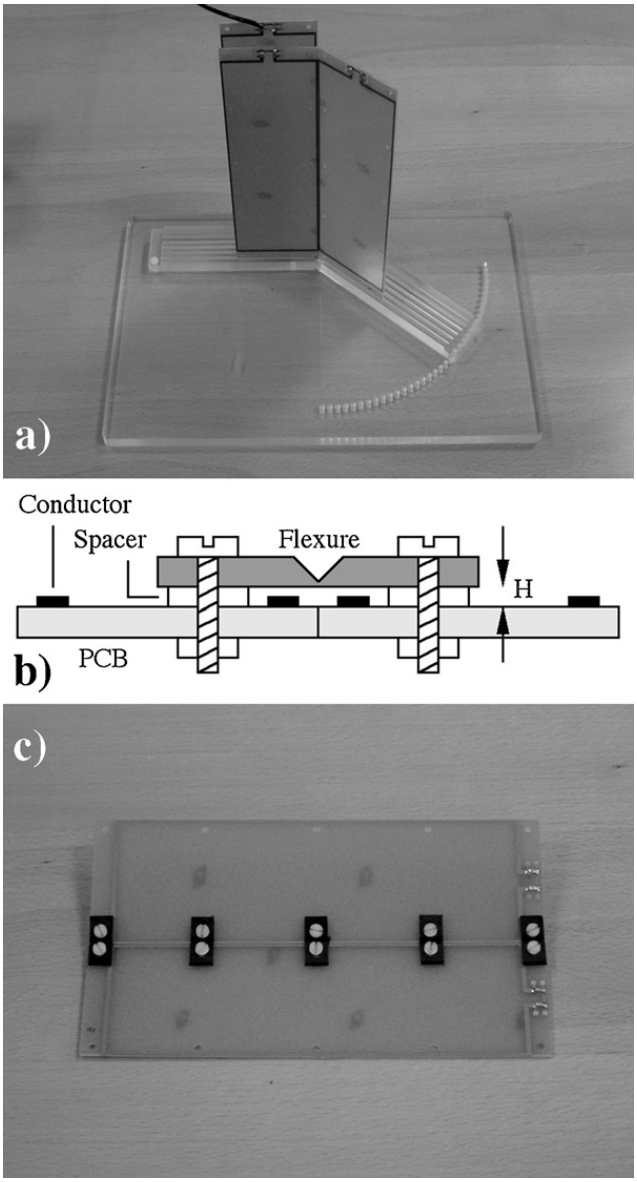

Fig. 6. (a) Arrangement for measuring coupling coefficient using an apex pivot, (b) flexure-based compensating pivot and (c) experimental PCB elements linked by flexures.

$\theta_0 = 45°$. The qualitative agreement with theory is again good. However, there are some differences that presumably arise from the planar conductor tracks, which distort the local magnetic field. In particular, thinner spacers than expected were required.

5.4. Ring resonators

Octagonal MI ring resonators were assembled from eight identical elements linked by flexures, as shown in Fig. 7a. Weakly coupled non-resonant inductive probes were attached on opposite sides of the ring for input and output coupling. The transfer characteristics of an undistorted ring were measured first. Fig. 8a shows the

frequency variation of the scattering coefficient S_{21}, which shows five sharp resonances as expected. The corresponding frequencies are superimposed on Fig. 4a. The agreement with first-order dispersion theory is good, and becomes excellent when second-neighbour effects are also considered.

The ring was then distorted symmetrically as shown in Fig. 7b, using asymmetric transducer positions to excite and detect all possible modes. The angle θ was found by geometry. Assuming that $S \gg R$, the 'diameter' D_{10} of an undistorted ring can be estimated as $D_{10} \approx S(1+\sqrt{2})$. For $S = 60$ mm, we obtain $D_{10} \approx 145$ mm. The corresponding 'diameter' D_1 of a distorted ring can be estimated in a similar way, allowing the angle to be extracted from measurements of D_1 and D_{10} as $\sin(\theta) = \{(1+\sqrt{2})(D_1/D_{10}) - 1\}/2$.

Transfer characteristics were measured with different amounts of distortion. For example, the frequency variation of S_{21} obtained for a coil distorted as shown in Fig. 7b is superimposed on Fig. 8a. There is significant splitting of the important primary resonance, but little

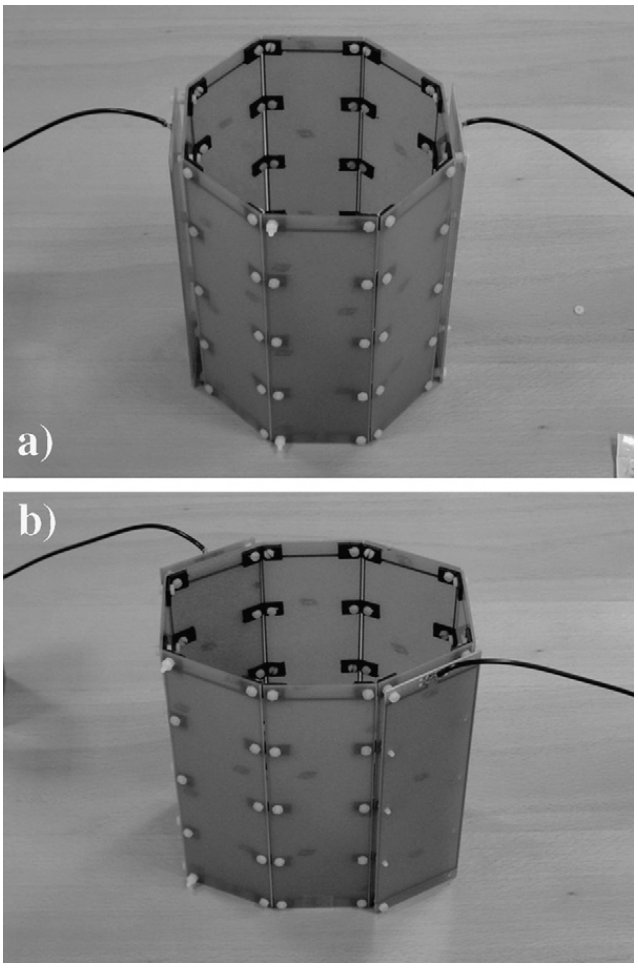

Fig. 7. Experimental realization of a PCB-based flexible octagonal magneto-inductive ring resonator: (a) undistorted and (b) distorted.

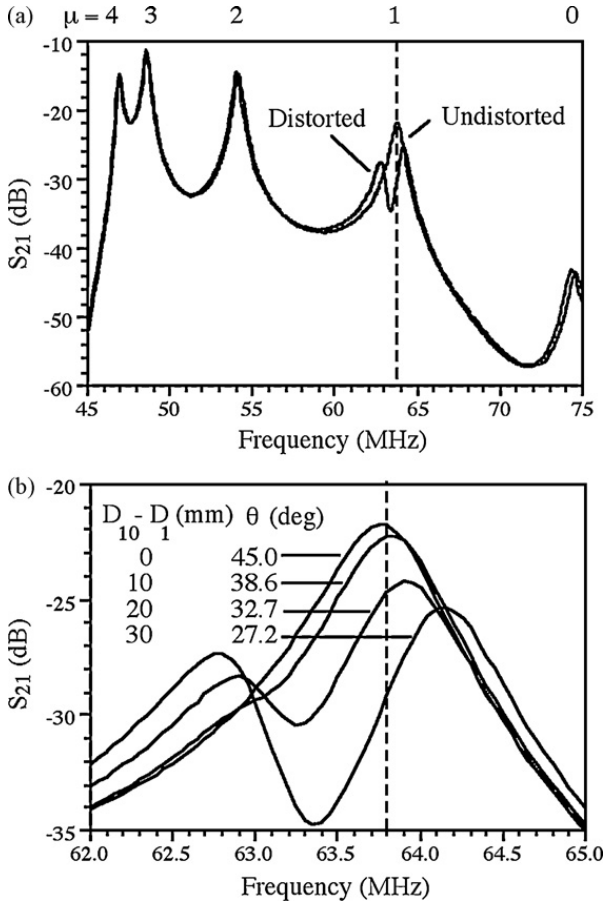

Fig. 8. (a) Experimental frequency variation of S_{21} of octagonal MI ring resonator, with and without distortion; (b) detailed variation in the vicinity of the primary resonance.

change in the other modes. Fig. 8b gives more detailed results, which show a systematic separation of the primary resonances (by up to 1.5 MHz) as the distortion $D_{10} - D_1$ is increased from zero and the angle θ is varied away from 45°. Only in the extreme case is the splitting effect significant.

The worst-case curve in Fig. 8b shows that the likely reduction in detected signal at 63.8 MHz frequency is just over 7 dB, when the ring is flexed so severely that the change in apex angle is $\Delta\theta = 27.2 - 45 = -17.8°$. Under more moderate conditions, when $\Delta\theta = 32.7 - 45 = -12.3°$, the likely reduction is less than 3 dB. These conditions confirm estimates in Section 3 that the hinge mechanism will stabilise nearest-neighbour coupling coefficients for angular changes of ±10°.

The variation of the two mode frequencies with θ extracted from this data is shown as superimposed on Fig. 5b. Again, there is reasonable agreement with the theoretical prediction for the compensating pivot, supporting the qualitative conclusions of the model.

6. Magnetic resonance imaging

In this section, we described the modifications needed to convert a MI ring resonator into a detector of MRI signals, and present the results of preliminary ^{1}H MRI experiments.

6.1. Detection of MRI signals

Two modifications are required to detect magnetic resonance signals. Firstly, the ring must be prevented from coupling directly to the excitation field created by the MRI scanner's powerful RF transmitter. Otherwise, large induced voltages are likely to destroy components such as capacitors. Even if they do not, the auxiliary field created by the detector will significantly modify the excitation profile. Secondly, detected signals must be efficiently extracted. Here we have used the approach in Fig. 9a, where, the single capacitor required for resonance is separated into three components, C_{T1} and C_{T2} and C_M. The first two effectively provide tuning, while the last allows connection of an impedance-matched tap.

Each resonant element is de-coupled from the excitation field using a diode-switched tank filter [47]. The tank is created from a pair of back-to-back diodes and a detuning inductor L_D formed from a short-circuited section of coaxial cable, which are placed in parallel with C_{T1}. During transmission, the diode voltage is high enough for conduction and the tank prevents circulation of large currents. During reception the diodes isolate L_D and normal resonant operation can take place. Signals are detected by connection of an output across C_M. Two taps are arranged at 90° around the ring, and their signals combined in-phase to detect a single running wave with the appropriate phase between elements. This approach provides greater uniformity than a single tap, which detects a standing wave [1].

Component values were determined by tuning each resonant element in isolation as follows. Paired sets of diodes (1N4148XTR; Fairchild Semiconductor) were used to achieve sufficient power handling from the passive de-coupling circuit. Unfortunately these and some other passive components displayed trace ferromagnetic properties. The value of C_{T1} was first fixed, and L_D was adjusted to tune the tank to 63.8 MHz frequency. C_{T2} and C_M and were then adjusted to achieve resonance and matching to 50 Ω impedance at this frequency. Finally, C_{T2} was adjusted again to lower the element resonant frequency to ≈53 MHz, the frequency known to place the primary resonance of an octagonal ring at 63.8 MHz. The ring was then assembled, equal length

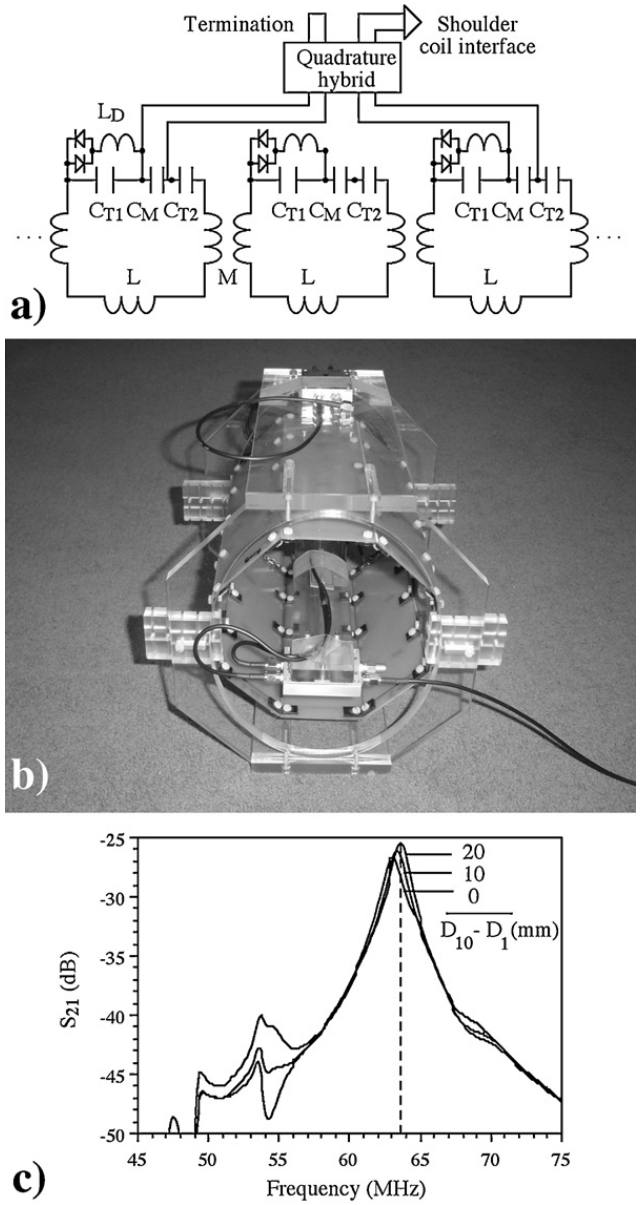

Fig. 9. (a) Circuit for detection of MR signals; (b) experimental detector, and (c) frequency variation of S_{21} obtained with rotating RF source and different distortions $D_{10} - D_1$.

tap cables were fitted, and C_{T2} and C_M were adjusted to optimise resonant frequency, impedance matching and balance. Tap signals were combined using a custom quadrature hybrid coupler (Emhiser Tele-Tech, Bozeman, MT), whose free port was terminated. The ring was mounted in a Perspex frame that allowed controllable adjustment of its shape as shown in Fig. 9b. The frame also contained an internal platform to allow a subject to be mounted for imaging without its weight distorting the ring.

MR signal detection was first simulated using a rotating dipole RF source, constructed from a pair of small rectangular crossed coils and fed via a second quadra-

ture hybrid coupler. This source is shown mounted on the central platform inside the MI ring in Fig. 9b. Depending on the connections to the exciting coils, this source can generate a field that rotates either clockwise or counter-clockwise. Similarly, depending on the connections of the taps, the ring can be arranged to detect one or other of the primary modes (1α or 1β).

Fig. 9c shows a measurement of the frequency variation of S_{21}, for different amounts of ring distortion $D_{10} - D_1$. For zero distortion, there is only a single peak near the MR operating frequency, the other modes having been largely suppressed using the selective quadrature detection mechanism. As $D_{10} - D_1$ increases, this peak does not split, but simply tracks to higher frequency, effectively following the behaviour of one of the split peaks in Fig. 8. Here, however, the peak height increases in the process, probably due to alterations in impedance matching. With the connections to both source and detector reversed, the peak tracked to lower frequency.

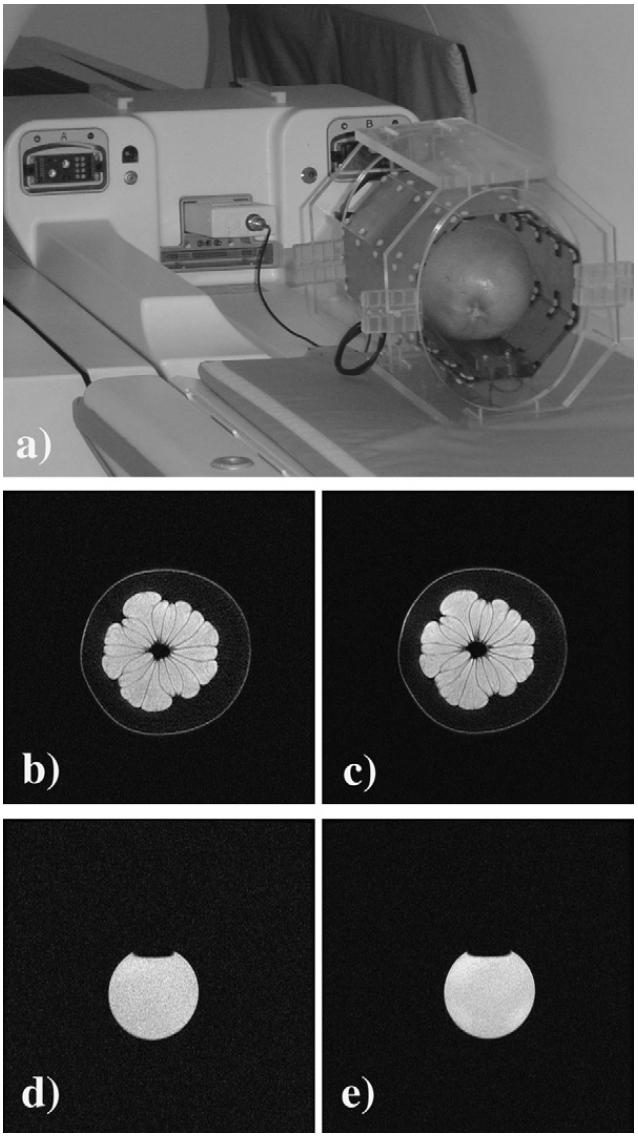

Fig. 10. (a) Arrangement for magnetic resonance imaging; (b and c) ^{1}H MR images of a pomelo fruit obtained from undistorted and distorted MI ring detector; (d and e) corresponding images from a 60 mm dia water-filled bottle.

Table 1
Sequence parameters for ^{1}H magnetic resonance imaging experiments.

Pulse sequence	Fast spin echo
Repetition time (TR)	800 ms
Echo time (TE)	90 ms
Echo train length	15
Flip angle	90°
Slice thickness	4 mm
Slice spacing	5 mm
Field of view (FOV)	200 mm
No. of excitations (NEX)	2

6.2. Magnetic resonance imaging

Preliminary ^{1}H magnetic resonance imaging was performed using a 1.5 T GE Signa Excite clinical scanner at St. Mary's Hospital, Paddington, London. The in-built body coil was used for excitation and the ring for reception only, with the signal from the quadrature hybrid passed into a single channel coil interface. The rotating dipole source was removed, and replaced with a test object, and the magnetoinductive ring was placed on the patient table with its axis parallel to the magnet bore as shown in Fig. 10a. The table was then translated into the magnet to position the ring at the isocentre. Imaging was carried out using a fast spin echo sequence with the parameters detailed in Table 1. Transmit parameters were first optimised using the scanner's auto pre-scan facility. No other adjustments were required, and good images were acquired immediately. The presence of some circuit components with trace ferromagnetism did not significantly modify the image, except in their immediate vicinity.

The first imaging subject was a pomelo (citrus maximus), a sweet grapefruit native to South-East Asia that is large enough to provide a good filling factor to the coil. Initial scans were carried out to identify a suitable sequence and to verify connections to the quadrature hybrid. The coil was then distorted symmetrically, so that its "diameter" D altered from its original value $D_{10} = 145$ mm by an amount $D_{10} - D = 30$ mm. This degree of distortion might be expected from prior electrical measurements to lead to a shift in resonant frequency that is large enough to degrade reception. Fig. 10 compares axial slice images obtained with the coil undis-

Table 2
Signal-to-noise ratios obtained from different imaging subjects, with different amounts of ring distortion.

	Measured signal-to-noise ratio (SNR)	
Coil profile ($D_{10} - D_1$)	Undistorted (0 mm)	Distorted (30 mm)
60 mm dia water bottle	28	42
85 mm dia water bottle	33	56

torted (Fig. 10b) and distorted (Fig. 10c). In each case, excellent detail may be seen, including the outer skin (bright), the thick inner skin (dark) and the segmented internal structure of the fruit. There is little difference between the images, despite any changes in electrical response. However, there is a difference in signal-to-noise ratio, as we show below. These results confirm that a magnetoinductive ring can indeed be used for signal detection in MRI, and that even a distorted coil may still provide useful imaging performance. These conclusions were confirmed by repetitively cycling the coil between undistorted and distorted states, and using other fruit subjects.

Image uniformity was then investigated using phantoms consisting of water-filled bottles with different diameters. Fig. 10 also compares axial slice images of a 60 mm diameter bottle obtained with the coil undistorted (Fig. 10d) and distorted (Fig. 10e) In each case, the cross-sections are uniformly bright, except for an air-bubble at the top. Images of a larger (85 mm diameter) bottle showed worse uniformity. However, no discernible pattern could be seen except slightly increased brightness where the subject most closely approached the resonant elements. Signal-to-noise ratio was investigated using the built-in image analysis software, which allowed extraction of the average signal values obtained in bright and dark regions over a circular area of adjustable diameter. The values obtained are detailed in Table 2, and lie in the range 28–33 for an undistorted coil, with a larger SNR being obtained for the larger subject. Importantly, the SNR increases to 42–56 when the coil is distorted, suggesting that the increased filling factor thus obtained has at least partially overcome any degradation of the coil's electrical performance. This result goes some way towards validating the original aim of the flexible coil concept.

7. Conclusions

A magnetoinductive waveguide is a periodic structure that supports waves propagating by magnetic coupling between *L–C* resonators. A polygonal MI ring resonator is analogous to the 'birdcage' coil used for detection in magnetic resonance imaging, but without rigid connections between adjacent elements. Here, we have considered the design of flexible MI rings constructed with mechanical links that allow adjacent resonant elements to rotate, which might be used to increase filling factor in head imaging.

A simple model based on parallel wire inductors has been used to estimate the mutual inductance between rectangular elements. Careful choice of the pivot location has been shown to render the nearest-neighbour coupling coefficient invariant to angular changes near the apex angle of an undistorted ring. Because nearest-neighbour coupling dominates the dispersion of MI waveguides, this in turn has allowed the resonant frequencies of the ring to be held approximately constant, independent of its shape. Performance is however degraded by the existence of higher-order coupling terms whose variations cannot be compensated in this way, and which cause a splitting of otherwise degenerate modes. Experiments have been conducted using PCB elements coupled by flexible hinges, and the invariance of the nearest-neighbour coupling has been confirmed. Given the sweeping nature of the approximations used, the qualitative agreement with theory is excellent. Differences are likely to lie in the approximate inductor shape assumed in the model and the neglect of 3rd and higher neighbour couplings. Octagonal ring resonators have been constructed, the mode spectra of regular and distorted rings have been determined, and the important primary resonance has been shown to split approximately as predicted.

Protection circuitry and a quadrature detection arrangement have been developed for magnetic resonance imaging, and preliminary ^{1}H imaging experiments have been carried out. The results are extremely encouraging, and show that high quality images may be obtained even from distorted coils, with a small increase in signal-to-noise ratio as filling factor improves. However, further work is required to determine the effect of ring distortion on imaging quality, and to identify mitigating design changes. For example, it is likely that some performance improvements can be achieved by increasing the relative strength of nearest-neighbour coupling terms and biasing the arrangement about an initially predistorted shape rather than a regular polygon. Finally, it is worth noting that there are additional applications of mechanical linkages that preserve nearest-neighbour coupling in the minimisation of reflection from bends in magnetoinductive waveguides. These will be important in achieving high performance in more general metamaterial circuits.

Acknowledgements

The authors are grateful to EPSRC for support under grant EP/D048389/1, to Professor Wady Gedroyc for allowing access to MRI facilities, to Mr Philip Jones for constructing CNC machined parts and flexure hinges and to Professor Ekaterina Shamonina and Dr Oleksiy Sydoruk of Erlangen University for valuable discussions.

References

[1] C.E. Hayes, W.A. Edelstein, J.F. Schenck, O.M. Mueller, M.J. Eash, An efficient, highly homogeneous radiofrequency coil for whole-body NMR imaging at 1.5 T, J. Magn. Reson. 63 (1985) 622–628.

[2] T. Vullo, R.T. Zipagan, R. Pascone, J.P. Whalen, P.T. Cahill, Experimental design and fabrication of birdcage resonators for magnetic resonance imaging, Magn. Reson. Med. 24 (1992) 243–252.

[3] B.J. Dardzinski, S.H. Li, C.M. Collins, G.D. Williams, M.B. Smith, A birdcage coil tuned by RF shielding for application at 9.4 T, J. Magn. Reson. 131 (1998) 32–38.

[4] G. Isaac, M.D. Schnall, R.E. Lenkinski, K. Vogele, A design for a double-tuned birdcage coil for use in an integrated MRI/MRS examination, J. Magn. Reson. 89 (1990) 41–50.

[5] G.B. Matson, P. Vermathen, T.C. Hill, A practical double-tuned $^{1}H/^{31}P$ quadrature birdcage headcoil optimized for ^{31}P operation, Magn. Reson. Med. 42 (1999) 173–182.

[6] T. Vullo, R. Pascone, R. Mancuso, R. Zipagan, P.T. Cahill, Transmission-line analysis of non-cylindrical birdcage resonators, Mag. Res. Imaging 12 (1994) 785–797.

[7] M.C. Leifer, Theory of the quadrature elliptic birdcage coil, Magn. Reson. Med. 38 (1997) 726–732.

[8] J. Tropp, The theory of the bird cage resonator, J. Magn. Reson. 82 (1989) 51–62.

[9] M.D. Harpen, Equivalent circuit for birdcage resonators, Magn. Reson. Med. 29 (1993) 263–268.

[10] M.C. Leifer, Resonant modes of the birdcage coil, J. Magn. Reson. 124 (1997) 51–60.

[11] J.T. Vaughan, G. Adriany, M. Garwood, E. Yacoub, T. Duong, L. DelaBarre, P. Andersen, K. Ugurbil, Detunable transverse electromagnetic (TEM) volume coil for high field NMR, Magn. Reson. Med. 47 (2002) 990–1000.

[12] J.T. Vaughan, G. Adriany, C.J. Snyder, J. Tian, T. Thiel, L. Bolinger, H. Liu, L. Delabarre, K. Ugurbil, Efficient high frequency body coil for high field MRI, Magn. Reson. Med. 52 (2004) 851–859.

[13] J.B. Pendry, A.J. Holden, D.J. Robbins, W.J. Stewart, Magnetism from conductors and enhanced nonlinear phenomena, IEEE Trans. Microwave Theory Tech. 47 (1999) 2075–2084.

[14] D.R. Smith, W.J. Padilla, D.C. Vier, S.C. Nemat-Nasser, S. Schultz, Composite medium with simultaneously negative permeability and permittivity, Phys. Rev. Lett. 84 (2000) 4184–4187.

[15] R. Marques, J. Martel, F. Mesa, F. Medina, Lefthanded-media simulation and transmission of EM waves in subwavelength split-ring-resonator loaded metallic waveguides, Phys. Rev. Lett. 89 (2002), 183901.

[16] H.O. Moser, B.D.F. Casse, O. Wilhelmi, B.T. Saw, Terahertz response of a microfabricated rod-split-ring-resonator electromagnetic metamaterial, Phys. Rev. Lett. 94 (2005), 063901.

[17] J.D. Baena, J. Bonache, F. Martin, R. Marques, F. Falcone, T. Lopetegi, M.A.G. Laso, J. Garcia-Garcia, M.F. Portillo, M. Sorolla, Equivalent-circuit models for split-ring resonators and complementary split-ring resonators coupled to planar transmission lines, IEEE Trans. Microwave Theory Tech. 53 (2005) 1451–1461.

[18] E. Shamonina, V.A. Kalinin, K.H. Ringhofer, L. Solymar, Magneto-inductive waveguide, Elect. Lett. 38 (2002) 371–373.

[19] M.C.K. Wiltshire, E. Shamonina, I.R. Young, L. Solymar, Dispersion characteristics of magneto-inductive waves: comparison between theory and experiment, Elect. Lett. 39 (2003) 215–217.

[20] E. Shamonina, L. Solymar, Magneto-inductive waves supported by metamaterial elements: components for a one-dimensional waveguide, J. Phys. D: Appl. Phys. 37 (2004) 362–367.

[21] M.C.K. Wiltshire, E. Shamonina, I.R. Young, L. Solymar, Experimental and theoretical study of magneto-inductive waves supported by one-dimensional arrays of 'swiss rolls', J. Appl. Phys. 95 (2004) 4488–4493.

[22] R.R. Syms, A. Young, I.R.L. Solymar, Low-loss magneto-inductive waveguides, J. Phys. D: Appl. Phys. 39 (2006) 3945–3951.

[23] R.R.A. Syms, O. Sydoruk, E. Shamonina, L. Solymar, Higher order interactions in magneto-inductive waveguides, Metamaterials 1 (2007) 44–51.

[24] A. Radkovskaya, O. Sydoruk, M. Shamonin, C.J. Stevens, G. Faulkner, D.J. Edwards, E. Shamonina, L. Solymar, Experimental study of a bi-periodic magneto-inductive waveguide: comparison with theory, IET Microwaves Antennas Propag. 1 (2007) 80–83.

[25] M.J. Freire, R. Marques, F. Medina, M.A.G. Laso, F. Martin, Planar magneto-inductive wave transducers: theory and applications, Appl. Phys. Lett. 85 (2004) 4439–4441.

[26] R.R.A. Syms, E. Shamonina, L. Solymar, Magneto-inductive waveguide devices, IEE Proc. Microwaves Antennas Propag. 153 (2006) 111–121.

[27] M.J. Freire, R. Marques, A planar magnetoinductive lens for 3D subwavelength imaging, Appl. Phys. Lett. 86 (2005), 182505.

[28] O. Sydoruk, M. Shamonin, A. Radkovskaya, O. Zhuromskyy, E. Shamonina, R. Trautner, C.J. Stevens, G. Faulkner, D.J. Edwards, L. Solymar, A mechanism of subwavelength imaging with bilayered magnetic metamaterials: theory and experiment, J. Appl. Phys. 101 (2007), 073903.

[29] L. Solymar, O. Zhuromskyy, O. Sydoruk, E. Shamonina, I.R. Young, R.R.A. Syms, Rotational resonance of magnetoinductive waves: basic concept and application to nuclear magnetic resonance, J. Appl. Phys. 99 (2006), 123908.

[30] O. Sydoruk, E. Shamonina, L. Solymar, Parametric amplification in coupled magnetoinductive waveguides, J. Phys. D: Appl. Phys. 40 (2007) 6879–6887.

[31] R.R.A. Syms, I.R. Young, L. Solymar, Three-frequency parametric amplification in magneto-inductive ring resonators, Metamaterials 2 (2008) 122–134.

[32] T. Floume, R.R.A. Syms, L. Solymar, M.R. Young, A practical parametric magneto-inductive ring detector, in: Proc. 3rd Metamaterials Conf., London, UK, August 30–September 4, 2009, pp. 132–134.

[33] G. Adriany, P.-F. Van de Moortele, J. Ritter, S. Moeller, E.J. Auerbach, C. Akgün, C.J. Snyder, T. Vaughan, K. Ugurbul, A geometrically adjustable 16-channel transmit/receive transmission line array for improved RF efficiency and parallel imaging performance at 7 Tesla, Magn. Reson. Med. 59 (2008) 590–597.

[34] R.R.A. Syms, I.R. Young, L. Solymar, Flexible magneto-inductive resonators and waveguides, in: Proc. 2nd Metamaterials Conf., Pamplona, Spain, September 22–26, 2008, pp. 45–47.
[35] R.R.A. Syms, I.R. Young, L. Solymar, Theory of distorted magneto-inductive ring resonators, in: Proc. 2nd Metamaterials Conf., Pamplona, Spain, September 22–26, 2008, pp. 635–637.
[36] M.C.K. Wiltshire, J.B. Pendry, I.R. Young, D.J. Larkman, D.J. Gilderdale, J.V. Hajnal, Preliminary evaluation of the application of high permeability microstructured material (μSM) in MRI, in: Proc. 9th Ann. Meet. Int. Soc. Mag. Res. Med., Glasgow, April 21–27, 2001, p. 1100.
[37] M.C.K. Wiltshire, J.B. Pendry, I.R. Young, D.J. Larkman, D.J. Gilderdale, J.V. Hajnal, Microstructured magnetic materials for RF flux guides in magnetic resonance imaging, Science 291 (2001) 849–851.
[38] M.C.K. Wiltshire, M.R. Henkelman, I.R. Young, J.V. Hajnal, Metamaterial yoke for signal reception – an initial investigation, in: Proc. 12th Ann. Meet. Int. Soc. Mag. Res. Med., Kyoto, May 15–21, 2004, p. 43.
[39] M. Allard, R.M. Henkelman, Using metamaterial yokes in NMR measurement, J. Magn. Res. 182 (2006) 200–207.
[40] M.C.K. Wiltshire, J.V. Hajnal, J.B. Pendry, D.J. Edwards, C.J. Stevens, Metamaterial endoscope for magnetic field transfer: near field imaging with magnetic wires, Opt. Express 11 (2003) 709–715.
[41] M. Freire, R. Marques, Near-field imaging in the megahertz range by strongly-coupled magneto-inductive surfaces, J. Appl. Phys. 100 (2006) 063105.
[42] M.J. Freire, R. Marques, L. Jelinek, Experimental demonstration of a $\mu = -1$ metamaterial lens for magnetic resonance imaging, Appl. Phys. Lett. 93 (2008) 231108.
[43] X. Radu, A. Lapeyronne, C. Craeye, Numerical and experimental analysis of a wire medium collimator for magnetic resonance imaging, Electromagnetics 28 (2008) 434–531.
[44] X. Radu, D. Garray, C. Craye, Toward a wire medium endoscope for MRI imaging, Metamaterials 3 (2009) 90–99.
[45] R.R.A. Syms, L. Solymar, M.R. Young, MR-safe cables – an application of magneto-inductive waves? in: Proc. 3rd Int. Cong. on Advanced Electromagnetic Materials in Microwaves and Optics, London, UK, August 30–September 4, 2009, pp. 221–223.
[46] R.R.A. Syms, L. Solymar, I.R. Young, Periodic analysis of MR-safe transmission lines IEEE J. Sel. Top. Quant. Elect. (2009), doi:10.11.09/JSTQE.2009.2032782.
[47] J.S. Hyde, R.J. Rilling, A. Jesmanowicz, Passive decoupling of surface coils by pole insertion, J. Magn. Reson. 89 (1990) 485–495.